PCCP

Enhanced Structural Stability of Formamidinium Lead Bromide ($FAPbBr_3$) Perovskites in Confined and Coated Configurations under Varying Pressures

Journal:	*Physical Chemistry Chemical Physics*
Manuscript ID	CP-ART-02-2025-000453.R1
Article Type:	Paper
Date Submitted by the Author:	28-Feb-2025

Complete List of Authors:	Nguyen, Hai Yen Thi; National Dong Hwa University, Department of Physics Nguyen, Duc Huy; National Dong Hwa University, Department of Physics Lai, Chien-Chih; National Dong Hwa University, Department of Physics and Department of Opto-Electronic Engineering Burba, Christopher; Northeastern State University, Department of Natural Sciences Chung, Yuan-Cheng; National Dong Hwa University, Department of Chemistry Chang, Hai-Chou; National Dong Hwa University, Department of Chemistry

Enhanced Structural Stability of Formamidinium Lead Bromide ($FAPbBr_3$) Perovskites in Confined and Coated Configurations under Varying Pressures

Hai Yen Thi Nguyen, Duc Huy Nguyen, Chien-Chih Lai[a]*, Christopher M. Burba[b*], Yuan-Cheng Chung[c], Hai-Chou Chang[c]*

AUTHOR INFORMATION

Corresponding Authors

Chien-Chih Lai – *Department of Physics, National Dong Hwa University, Shoufeng, Hualien 974, Taiwan;* Email: cclai@gms.ndhu.edu.tw

Hai-Chou Chang – *Department of Chemistry, National Dong Hwa University, Shoufeng, Hualien 974, Taiwan;* Email: hcchang@gms.ndhu.edu.tw

Christopher M. Burba – *Department of Physical Sciences, Northeastern State University, Tahlequah, OK, USA;* Email: burba@nsuok.edu

Authors

Hai Yen Thi Nguyen – *Department of Physics, National Dong Hwa University, Shoufeng, Hualien 974, Taiwan;* Email: nguyenthihaiyen.jenny.04@gmail.com

Duc Huy Nguyen – *Department of Physics, National Dong Hwa University, Shoufeng, Hualien 974, Taiwan;* Email: nd.huy.nd@gmail.com

Yuan-Cheng Chung – *Department of Chemistry, National Dong Hwa University, Shoufeng, Hualien 974, Taiwan;* Email: 611012109@gms.ndhu.edu.tw

Keywords

lead bromide pervoskites, photoluminescence, phase transitions, high pressure, infrared spectroscopy

Abstract

Formamidinium lead bromide ($FAPbBr_3$) perovskites are a rapidly emerging class of materials that have the potential to revolutionize optoelectronic and photovoltaic industries. It is now recognized that $FAPbBr_3$ photoelectronic properties are strongly influenced by the underlying perovskite structure, with static and dynamic disorder among the lattice sites playing prominent roles. We show how these structure-property interactions may be exploited to enhance the photoluminescent properties of $FAPbBr_3$ by increasing the relative amount of $FAPbBr_3$ that is exposed to the surface of a substrate material. For example, encapsulating $FAPbBr_3$ inside the nanopores of a poly(ether ether ketone) (PEEK) membrane or coating it on a yttrium aluminum garnet (YAG) fiber increases photoluminescence stability by a factor of at least 16. $FAPbBr_3$ in these different

configurations is then examined with isothermal, pressure-dependent infrared spectroscopy to better understand the origin of this enhancement. In its bulk form, $FAPbBr_3$ undergoes two discernible pressure-induced phase transitions at approximately 0.7 and 1.8 GPa, leading to notable red shifts in NH_2 stretching and bending band wavenumbers of the FA^+ cations. However, confined and coated forms of $FAPbBr_3$ experience reduced amounts of band shifting across these phase transition pressures. These differences point to some degree of structural stabilization (at least from the perspective of the FA^+ cations) upon pressurization.

Introduction

Significant efforts have been made to develop optoelectronic devices by advancing our understanding of the interplay between photonics and electronics. To this end, organic-inorganic hybrid lead halide perovskites have garnered attention for their potential use in photoelectric devices and all-optical photonic circuits.[1–11] Hybrid perovskites deliver high band gaps with tunable ranges from ultraviolet to near infrared wavelengths, making these materials ideal candidates as light absorbers in solar cells or light-emitting diode and laser applications.[12–14] Indeed, perovskite solar cells now have power conversion efficiencies that exceed 25% and are competitive with silicon-based counterparts.[15,16] Despite these attractive qualities, questions surrounding the long-term stability of hybrid perovskites remains a key factor limiting widespread applications and device performance.

Hybrid lead halide perovskites have a general structure of $APbX_3$, where the A site is occupied by either a methylammonium (MA) or formamidinium (FA) cation and X is a halide anion. The room temperature crystal structure belongs to the cubic $Pm\overline{3}m$ space group (No. 221). However, anharmonic psuedorotations and distortions of the PbX_6^{2-} octahedral units create dynamic and static distortions in the crystal that impacts the optoelectronic properties of the materials.[17–22] The bulky nature of the FA molecule also mitigates long-range translational registry across the A sites, leading to disorder among the FA ions that remains present even at low temperatures.

$FAPbBr_3$ experiences two phase transformations upon cooling;[23] these follow the general octahedral tilting paradigm given by Glazer.[24,25] The $Pm\overline{3}m$ phase persists to ~275 K after which $FAPbBr_3$ adopts a tetragonal *P4/mbm* (No. 127) phase. This is followed by a second phase transition at ~150 K to orthorhombic *Pnma* (No. 62). High pressure also induces phase changes in the perovskite structure.[26,27] For instance, the ambient pressure $Pm\overline{3}m$ phase converts into a 2×2×2 cubic supercell belonging to the $Im\overline{3}$ space group (No. 204) at 0.53 GPa. This is followed by an orthorhombic distortion at 2.2 GPa, where $FAPbBr_3$ adopts a *Pnma* crystal structure. Higher pressure (>4 GPa) leads to amorphization of the compound. The structural changes found in the XRD experiments are confirmed with

pressure-dependent Raman spectroscopy, albeit with slightly different phase transition pressures.[28]

In spite of the high research interest centered on $FAPbBr_3$, the majority of the studies have focused on elucidating structure-property maps for the pure material under ambient pressure conditions. Information about $FAPbBr_3$ in different shape and confinement modalities is relatively scarce in spite of the tremendous opportunities these simple modifications offer for tuning $FAPbBr_3$ properties. For example, the operational temperature of continuous-wave perovskite lasers is typically confined to cryogenic levels due to the short lifetime and thermal instability of metal halide perovskites.[2] Our prior research has shown that coating perovskite onto a high-quality crystal fiber can enhance the thermal stability of metal halide perovskites.[1] By controlling the shape, size, and crystallinity of these materials, one can effectively prevent perovskite degradation, achieving improved long-term stability.[2–4] Similarly, emissions with a notable shift in frequency were noted when perovskites were placed inside the nanopore structure of anodic aluminum oxide (AAO) or porous silicon.[29,30] Encapsulation led to enhanced stability through a quantum confinement effect, which adjusts the bandgap and ensures photoluminescent stability when a metal halide perovskite is confined at the nanoscale.

We aim to address this critical knowledge gap by examining $FAPbBr_3$ when it is coated on yttrium aluminum garnet (YAG) fibers or confined inside a nanoporous matrix of poly(ether ether ketone) (PEEK). PEEK is a durable thermoplastic polymer with outstanding physicochemical and tribological characteristics,[31] making it an excellent choice for chemical processing, electronics, and biomedical applications. For instance, creating high-quality porous PEEK with suitable pore size and porosity is essential for developing patient-specific PEEK bone implants in orthopedics.[32] Electrochemical applications of PEEK are widespread, including battery separators,[33–35] fuel cells,[36] and high temperature capacitors.[37] Despite the widespread use of porous PEEK in various industries, studies on metal halide perovskites confined in the pores of porous PEEK membranes are lacking.

The phase behavior of $FAPbBr_3$ in coated and confined configurations is evaluated with pressure-dependent infrared spectroscopy, which is an excellent technique for probing solid-state phase transitions and confinement effects in a wide range of material types.[27,38–40] Isothermal pressurization increases the density of a compound and has the effect of reducing the average distance between molecular species. The net effect is an enhancement in intermolecular (or interionic) interactions, which become manifested as wavenumber shifts in the vibrational modes. In this way, high pressure spectroscopic experiments can accentuate and reveal subtle interaction motifs that are often missed in ambient pressure spectra. For example, confinement effects on ionic liquids (ILs) within nanopores of AAO experience structural reorganizations among the ionic species upon pressurization that are not mimicked by ambient conditions.[40] The interactions between ions and pore surfaces

appear to play a significant role in altering the pressure-induced phase-transition behaviors of confined ionic compounds. Vibrational spectroscopic studies are particularly valuable for $FAPbBr_3$ as structural disorder is an important feature of these materials. Infrared spectroscopic experiments can provide information about XRD-silent disordered domains and clarify how those regions respond to high pressure when $FAPbBr_3$ is in coated and confined configurations.

Experimental Methods

Compound abbreviations, chemical suppliers, and product purities for the various ingredients used to prepare the formamidinium lead bromide ($FAPbBr_3$) samples are summarized in Table 1. $FAPbBr_3$ was synthesized through a similar method used in previous publications,[1,41] where separate solutions of FABr and $PbBr_2$ are mixed to create the $FAPbBr_3$ pervoskite. This method allowed for the easy impregnation of $FAPbBr_3$ in the pore structure of the PEEK polymer and dip coating of the YAG optical fibers. To this end, $PbBr_2$ (0.088 g) was dissolved in a 1:1 (v/v) DMF/DMSO solution (200 µL) and heated to 100°C to form a $PbBr_2$ solution. The FABr solution (0.05 M) was prepared by dissolving FABr in isopropyl alcohol at 60°C. The chemical structure of the formamidinium cation is presented in Figure 1.

Table 1. Reagent list for the various compounds used in this study.

Compound (Abbreviation)	Vendor	Purity	CAS Number
Formamidinium bromide (FABr)	Sigma Aldrich	98%	146958-06-7
Lead(II) bromide	Sigma Aldrich	99.999%	10031-22-8
Dimethylformamide (DMF)	Thermo Fisher	99.8%	68-12-2
Dimethyl sulfoxide (DMSO)	J.T. Baker	99.9%	67-68-5
Isopropyl alcohol	J.T. Baker	99.5%	67-63-0

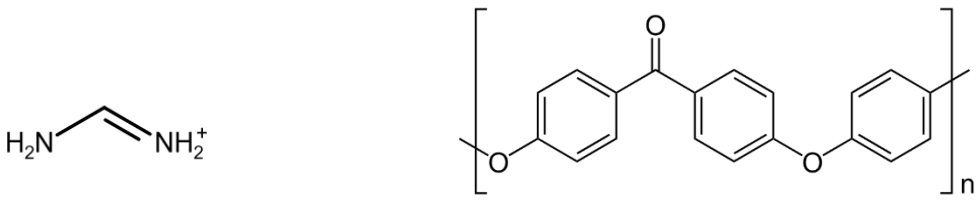

Figure 1. Chemical structures of the formamidinium cation (left) and PEEK (right).

Poly(ether ether ketone) membranes (PEEK, structure provided in Figure 1) with a pore size of 5 nm and a thickness of 50 µm were procured from Redoxme AB, Sweden. The PEEK membrane was washed multiple times with isopropyl alcohol to remove any impurities, as confirmed by IR absorption analysis. Growth of the $FAPbBr_3$ compound was

accomplished by immersing either the PEEK membrane or YAG optical fiber in the $PbBr_2$ solution for a minimum of 5 min. The surfaces were then cleaned to remove any $PbBr_2$ residue, and after drying, the samples were inserted into the FABr solution. This is followed by annealing at 80°C. For sake of communication, we refer to $FAPbBr_3$ impregnated in the PEEK membrane or coated onto the YAG fiber as $FAPbBr_3$@PEEK and $FAPbBr_3$@YAG, respectively. Optical microscopy (Nikon LV100) and transmission electron microscopy (FEI Tecnai G^2 F20) was used to image the $FAPbBr_3$ layer on the YAG fiber. Elemental mapping of the $FAPbBr_3$ surface layer was accomplished by energy dispersive X-ray spectroscopy. Prior to TEM imaging, the sample was coated with poly(methyl methacrylate) (PMMA) and platinum layers to make the sample electrically conductive and protect it from the ion beam.

Photostability was assessed through luminescence intensity measurements. The excitation source was a continuous-wave laser with a wavelength of 405 nm and a power of 1 μW. The laser beam was focused onto the sample through a 10× objective lens of a confocal microscope. A long-pass optical filter was used to remove Rayleigh scattered electromagnetic radiation at 405 nm, while the remaining emitted light (photoluminescence) was focus into an optical fiber. Two-dimensional scans of the sample surfaces provided information about the spatial distribution of the photoluminescent properties. This information was obtained with either a Newport UV enhanced silicon photodetector (818-UV/DB), a photomultiplier tube (PMT), or a spectrometer equipped with a CCD detector. Photoluminescent intensity was also measured across all emitted wavelengths to yield the total luminescent intensity. In this case, the single point exposure time was set to 0.128 ms. Spectroscopic scanning of the emitted radiation at a specific point used a 100 ms exposure time.

The $FAPbBr_3$ samples were subjected to high pressure with a diamond anvil cell (DAC) equipped with two type-IIa diamonds. Calcium fluoride crystals were positioned in a 0.3-mm-diameter hole of a 0.25-mm-thick Iconel gasket. In brief, this entailed compressing the CaF_2 in the gasket to create an IR-transparent disc. A needle was then used to scratch out the CaF_2 surface for solid $FAPbBr_3$ powder deposition, followed by more CaF_2. A second round of compression created a visibly opaque layer that was transparent to IR radiation and ready for high pressure experiments. The $FAPbBr_3$@PEEK and $FAPbBr_3$@YAG sample preparation steps were similar: small pieces of the samples were cut and positioned between CaF_2 layers. The CaF_2 serves two purposes. First, it functions as a pressure-transmitting medium. Second, it reduces the amount of sample in the beam path, which is necessary to avoid saturation of the absorption bands in transmission spectroscopy. It is very difficult to observe spectroscopic changes when bands are over absorbed. Pressure calibration followed Wong's method.[42,43] Infrared spectra were recorded using a Fourier-transform spectrometer (Perkin-Elmer RXI) equipped with a beam condenser. Band center

uncertainties are less than 1 cm^{-1}.

Vibrational mode calculations on the FA^+ cation were performed with the Orca computational package (version 5.0.4).[44–46] Integral calculations were performed with Shark[47] and the Libint library[48]. The calculations were carried out with density functional theory (DFT), using Becke's three-parameter hybrid exchange functional[49] and the Lee–Yang–Parr correlation functional[50,51] (B3LYP). The def2-TZVPP triple-ζ basis set with two sets of polarization functions was used for all calculations.[52] A self-consistent field (SCF) was established with Pulay's direct inversion in iterative subspace (DIIS) technique.[53,54] The energy error threshold for initiating DIIS was 0.2 Hartree, and the maximum size of the DIIS linear equations was five. DIIS error is 1 x 10^{-8} Hartree. Extreme convergence criteria (energy changes of less than 1.0 x 10^{-12} Hartree) were applied for SCF construction. Anharmonicity in the vibrational modes was modeled with second-order vibrational perturbation theory (VPT2).[55] The anharmonic displacement was set to 0.050 with a Hessian cutoff of 1 x 10^{-12}. Vibrational mode linear decomposition was accomplished with the vibAnalysis software package.[56]

RESULTS AND DISCUSSION

Ambient Pressure IR Spectroscopy

The response of $FAPbBr_3$ to high pressure is evaluated from the intramolecular vibrations of the FA^+ ion, which produce strong IR absorptions in the mid-IR region. Molecular entities in crystalline environments often exhibit vibrational mode splitting and changes in mode spectral activity due to the site group and unit cell group symmetries of the crystal. Under ambient pressure and temperature conditions, the FA^+ ions occupy octahedral 1b Wyckoff sites of the $Pm\bar{3}m$ space group with considerable amounts of disorder among the FA^+ cations. For these reasons, vibrational modes involving the FA^+ cation are often described in terms of an "isolated" species instead of using the formally correct factor group analysis.[20,57,58] Isolated FA^+ ions belong to the C_{2v} point group symmetry, and the normal modes of vibration for the ion may be classified according to the irreducible representations of this point group: $\Gamma = 7A_1 + 2A_2 + 6B_1 + 3B_2$. IR active modes have A_1, B_1, and B_2 irreducible representations.

Ambient-pressure infrared spectra of $FAPbBr_3$ in various configurations are presented in Figure 2. Two spectroscopic regions are examined to understand how FA^+ responds to pressure. First, we examine a characteristic band at 1717 cm^{-1}. Kucharska et al. assign this band to a mixture of atomic motions, including in-plane NH_2 scissoring (δNH_2, 50% potential energy distribution, PED), CN antisymmetric stretching ($\nu_{as}CN$, 40% PED), and in-plane CH bending (δCH, 10% PED).[5–7,57] Vibrational mode linear decomposition using our own B3LYP/def2- TZVPP calculations paint a similar picture. To simplify communication, we will simply refer to this band as the "$\delta NH_2/\nu_{as}CN$" mode. Figures 2b and 2c also display bands at

approximately 1597 and 1647 cm^{-1} that may be attributed to vibrations of the benzene ring and ketone groups of PEEK, respectively.[59] Fortunately, these bands are well separated from the 1717 cm^{-1} band and do not interfere with our ability to monitor changes to the FA^+ cations from this spectroscopic point of view. The 1717 cm^{-1} band remains at a similar wavenumber in Figures 2a-c, suggesting that IR measurements under ambient pressure lack sufficient sensitivity to distinguish local structural changes (as measured from the perspective of the $\delta NH_2/\nu_{as}CN$ mode) that are induced by the presence of PEEK and YAG optical fiber.

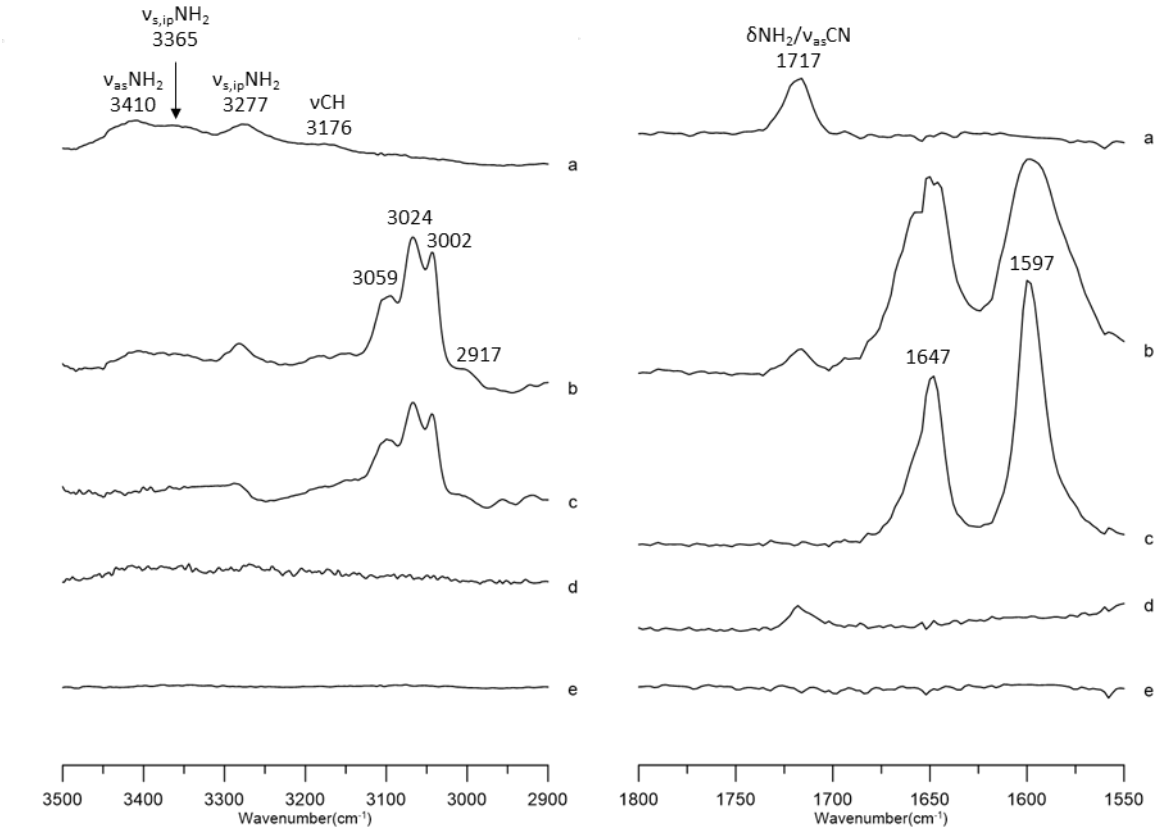

Figure 2. Ambient-pressure infrared spectra of (a) pure $FAPbBr_3$, (b) $FAPbBr_3$@PEEK, (c) PEEK, (d) $FAPbBr_3$@YAG fiber, and (e) YAG fiber.

The second spectroscopic region we explore (3500–2900 cm^{-1}) contains NH and CH stretching bands of the cation. These features are also presented in Figure 2. Ambient-pressure infrared spectra of pure $FAPbBr_3$ has absorption bands at 3410, 3365, 3277, and 3176 cm^{-1}. The FA^+ cation contains two primary amine groups on either side of the molecule; these moieties may each produce symmetric and antisymmetric NH stretching motions. Anharmonic vibrational mode calculations at the B3LYP/6-311G(2d,2p) level of theory predict four NH stretching modes, but the two highest energy modes have nearly equal wavenumbers and mainly consist of antisymmetric stretches of isolated NH_2 groups,

$\nu_{as}NH_2$.[57] These modes are assigned to the 3410 cm^{-1} band. The $\nu_{as}NH_2$ modes are followed by in-phase and out-of-phase symmetric stretching motions of the two NH_2 groups ($\nu_{s,ip}NH_2$ and $\nu_{s,op}NH_2$, respectively), which are assigned to the 3365 and 3277 cm^{-1} bands, respectively. The anharmonic calculations somewhat overestimate the N–H stretching wavenumbers. A small 0.964–0.984 scaling factor brings these values into agreement with the experimental data. The single CH stretching mode, vCH, is attributed to the 3176 cm^{-1} band. The harmonic DFT calculations accurately reproduces this band (3202 cm^{-1}) with a 0.992 scaling factor, whereas the anharmonic calculation overestimates this band's wavenumber by 3.0%.

These assignments are supported by our own relative intensity calculations for these modes (Table 2). As previously noted, the two $\nu_{as}NH_2$ modes have essentially the same calculated frequency. Summing the calculated intensities for these two modes gives a total intensity of 284 km mol^{-1}, which is comparable to the calculated intensity of the $\nu_{s,op}NH_2$ mode (300 km mol^{-1}). Furthermore, the $\nu_{s,ip}NH_2$ mode at 3365 cm^{-1} has a calculated intensity of 44 km mol^{-1}, and vCH has a very low calculated intensity (6.7 km mol^{-1}). The progression of these mode intensities is in excellent agreement with the observed experimental relative intensities displayed in Figure 2 for these bands.

Further support for assigning the 3176 cm^{-1} band to vCH is available from the spectroscopic literature on imidazolium-based ionic liquids. The FA^+ ion is structurally similar to the N–C–N fragment of the imidazolium ring. In those systems, the hydrogen atom bonded to the bridging carbon atom between the two N atoms produces a characteristic IR band at approximately 3160 cm^{-1}, which is quite close to the 3176 cm^{-1} band found here.[60–63]

Table 2. Harmonic and anharmonic vibrational mode wavenumbers (cm^{-1}) and intensities (km mol^{-1}) for the FA^+ ion calculated at the B3LYP/def2-TZVPP level of theory.

Vibrational Mode	Irreducible Representation	ν_{harm}	ν_{ahrm}	IR Intensity
1	A_1	519	521	0.6
2	A_2	547	541	0.0
3	A_2	606	613	0.0
4	B_2	630	641	423.4
5	B_2	720	704	13.9
6	B_1	1042	1021	0.5
7	B_2	1085	1059	17.0
8	A_1	1127	1114	3.5
9	B_1	1386	1372	60.8
10	A_1	1413	1378	8.5

11	B_1	1617	1565	7.9
12	A_1	1693	1656	39.9
13	B_1	1767	1722	423.0
14	A_1	3202	3083	6.7
15	B_1	3539	3399	300.4
16	A_1	3553	3420	44.3
17	B_1	3656	3484	99.1
18	A_1	3657	3484	184.8

High Pressure IR Spectroscopy

Infrared spectra of $FAPbBr_3$ are presented as a function of applied pressure in Figure 3. The $\delta NH_2/\nu_{as}CN$ band experiences minimal changes in absorption frequency and bandwidth between ambient pressure and 0.7 GPa. However, the band gains a low frequency shoulder when pressures exceed 1.1 GPa. Higher pressure causes a marked decrease in band center frequency and obvious broadening of the band. Changes in the $\delta NH_2/\nu_{as}CN$ band are mirrored by a similar progression in the NH stretching modes, where the bands experience relatively mild changes up to 1.5 GPa followed by red shifting and broadening with higher amounts of compression. Under a pressure of 2.5 GPa, the $\nu_{as}NH_2$ and $\nu_{s,op}NH_2$ modes shift from 3410 and 3277 cm^{-1} at ambient pressure to 3365 and 3228 cm^{-1}, respectively.

X-ray diffraction experiments reveal two phase transformations in $FAPbBr_3$ across this pressure range.[26,28] The first transition (cubic $Pm\bar{3}m$ → cubic $Im\bar{3}$ at 0.53 GPa) produces minor spectroscopic changes in our infrared spectra, indicating the local environment about the FA^+ cations is comparable in the two phases. However, the orthorhombic distortion inherent to the second phase transformation ($Im\bar{3}$ → *Pnma* at 2.2 GPa) triggers an abrupt change in the spectroscopic signature of the cation. This is traced to the uniquely different cationic environments in this phase that are absent in the lower pressure forms of $FAPbBr_3$. The reversibility of the $FAPbBr_3$ structures, at least from the perspective of the FA^+ cationic local structures, is confirmed by full recovery of the spectral features after pressure cycling back to ambient pressure.

All of the νNH_2 bands experience some degree of red shifting with applied pressure. Moreover, the 1717 cm^{-1} band has a large amount of δNH_2 character, which makes this band also sensitive to changes in the NH_2 coordination environment. Red shifts in N–H stretching modes are commonly encountered in amine-based systems because of the propensity of the NH functional group to form hydrogen bonds. The strength of the hydrogen bond is coupled to the coordinative interaction strength between the hydrogen bond donor and acceptor species. Strong hydrogen bonds cause a lengthening of the N–H bond and a red shift in its mode frequency. In $FAPbBr_3$, the FA^+ cations occupy sites defined

by neighboring $PbBr_6$ octahedra. Bromide ions may function as Lewis bases capable of coordinating the N–H groups. Our pressure-dependent IR data clearly show these weak N–H···Br hydrogen bonds are strengthened when $FAPbBr_3$ is placed under elevated pressures, and these changes are reversible up to 2.5 GPa.

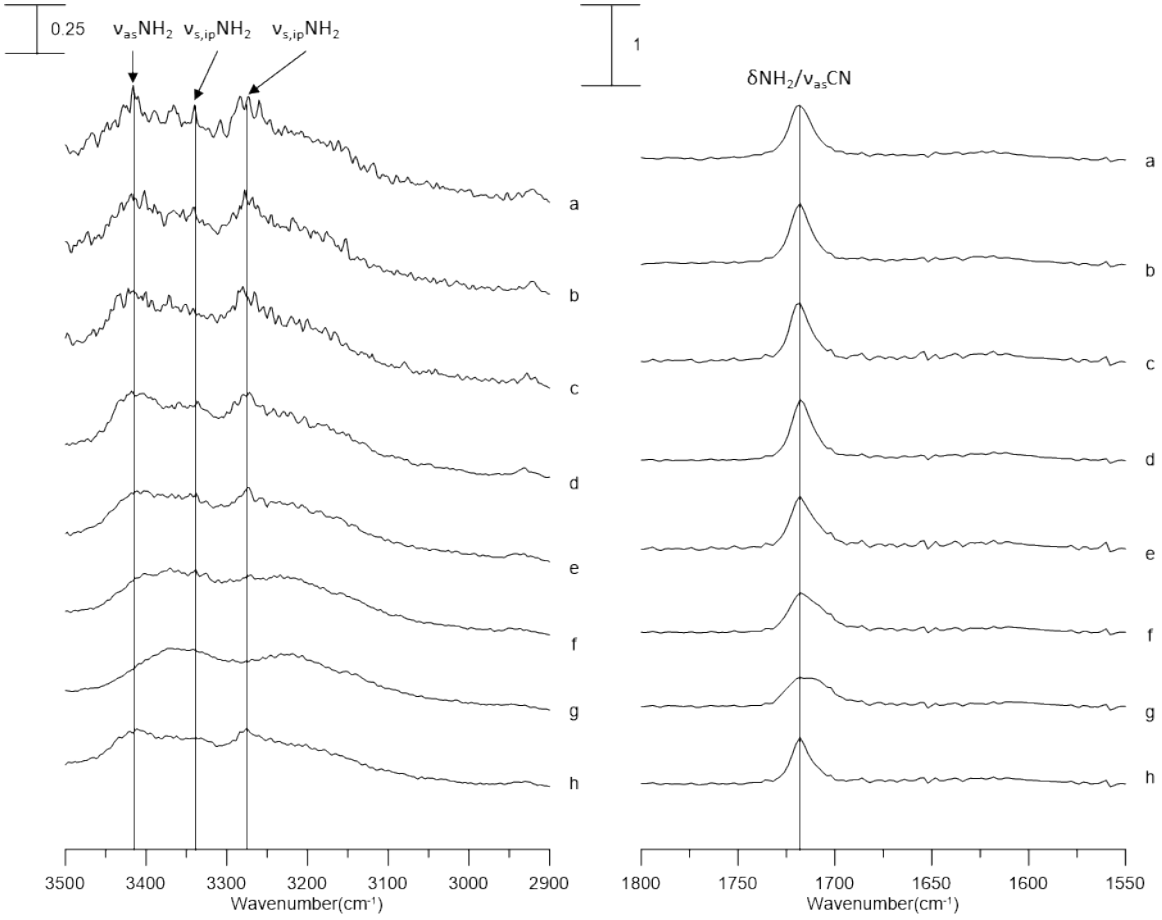

Figure 3. IR spectra of pure $FAPbBr_3$ at the pressure of (a) ambient, (b) 0.4, (c) 0.7, (d) 1.1, (e) 1.5, (f) 1.8, (g) 2.5 GPa, and (h) pressure cycling back to ambient. A relative intensity scale is provided in the upper left part of each panel.

Pressurization to 2.5 GPa and subsequent depressurization to ambient conditions improves the signal-to-noise ratio (cf. Figure 3a to 3h). We believe this is related to the experimental configuration of the diamond anvil cell used to measure the pressure-dependent, transmission IR spectra. Samples are placed inside a 0.25-mm-diameter hole of an Inconel of gasket and then compressed between two diamonds. The small size of hole restricts the amount of the IR beam that may pass through the sample, leading to relatively low signal-to-noise ratios. Applied pressure causes an irreversible structural change to the gasket, and the diameter of the hole increases in size. This is because the gasket experiences plastic-like deformations and is unable to recover its initial shape. The net effect is a higher amount of the IR radiation is able to pass through sample, which increases the signal-to-

noise ratio. It is also possible that compression to 2.5 GPa thins the sample, which will enhance its overall transparency. This will further increase the sensitivity of the transmission IR spectroscopic experiment. We also note that IR sources are black-body radiators that are optimized to have the highest IR intensity emission at the center of the mid-IR region. Thus, bands in the 1550-1800 cm^{-1} naturally experience a greater flux of IR radiation than the 2900-3500 cm^{-1}.

Figure 4 showcases the infrared spectra of $FAPbBr_3$ when it is encapsulated in a PEEK membrane ($FAPbBr_3$@PEEK). The pressure ascends from ambient conditions to 2.5 GPa in the figure. New absorption bands from the PEEK membrane appear in the IR spectra and partially overlap the $\delta NH_2/\nu_{as}CN$ band. In spite of this complication, the $\delta NH_2/\nu_{as}CN$ band wavenumber is relatively insensitive to compression, and the band width does not appear to broaden above 1.8 GPa as it does for unconfined $FAPbBr_3$. Additional insights may be gathered from the νNH_2 bands (3500–2900 cm^{-1}). Again, the PEEK membrane produces new absorption bands in the 3050–3150 cm^{-1} range, which are attributed to aromatic C–H stretching vibrations. These new bands are relatively well separated from the νNH_2 features and do not impact our ability to track changes in the FA^+ ions from the perspective of these modes. We do note, however, that these PEEK νCH bands experience large red shifts when the samples are placed under high pressure. This implies the PEEK membrane is affected by the pressurization process. In contrast, the $\nu_{as}NH_2$ band at approximately 3410 cm^{-1} exhibits gradual band wavenumber shifts as the pressure increases from ambient to 1.8 GPa, along with mild changes in band width. The $\nu_{s,op}NH_2$ band intensity also becomes diminished when the sample is pressurized to 2.5 GPa.

Confinement is often associated with structural changes to the confined materials. This is because a confined substance experiences a relatively large interfacial region, and the coordinative interactions available with the pore wall are absent in the pure phases. Furthermore, the constricted space inside narrow pores can frustrate crystallization, which increases the quantities of amorphous domains. Finally, bulk-like regions in the centers of the nanopores may experience limitations in the diverging correlation length that serve to alter the critical pressure for phase change. Ambient pressure IR spectra of $FAPbBr_3$@PEEK is comparable to that of $FAPbBr_3$, implying that the ambient pressure $FAPbBr_3$ structure is retained when it is embedded in PEEK. However, there are subtle differences in how the two samples respond to applied pressure. While both samples experience red shifts in the νNH_2 bands above 1.5 GPa, the $\delta NH_2/\nu_{as}CN$ band for $FAPbBr_3$@PEEK does not appear to follow the same trajectory as $FAPbBr_3$. One possible interpretation of this change is that $FAPbBr_3$ experiences some degree of structural stabilization when it is encapsulated in PEEK nanopores. Even though the relative contributions from core (bulk-like) and surface (contact or close to surface) impacts on pressure induced phase transformations cannot be elucidated from dataset, it is clear that this confinement effect, prominently evident under

high pressures, is not discernible under ambient pressure conditions.

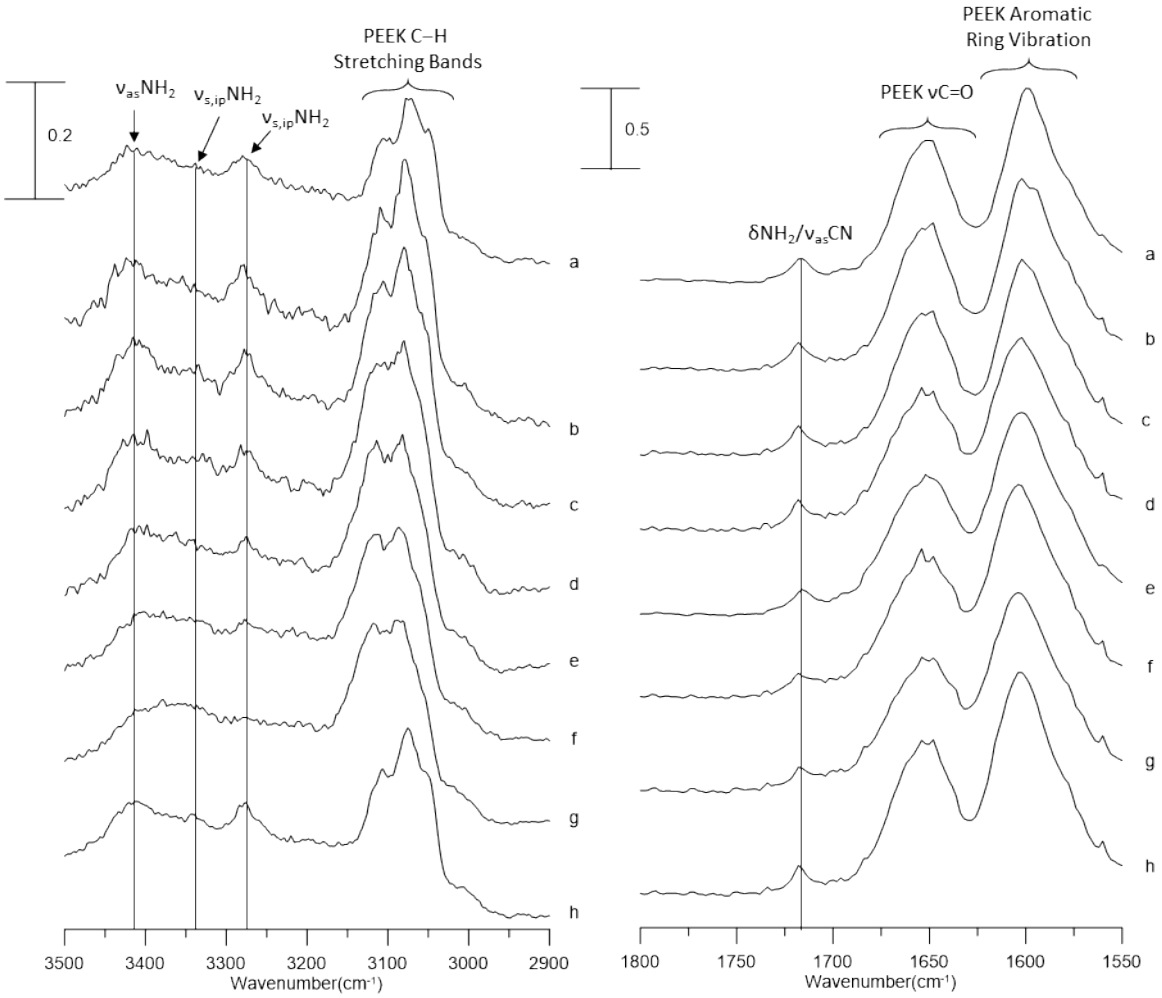

Figure 4. IR spectra of $FAPbBr_3$@PEEK at the pressure of (a) ambient, (b) 0.4, (c) 0.7, (d) 1.1, (e) 1.5, (f) 1.8, (g) 2.5 GPa, and (h) pressure cycling back to ambient. A relative intensity scale is provided in the upper left part of each panel.

In a complimentary experiment, $FAPbBr_3$ is coated onto a 50-μm-diameter yttrium aluminum garnet (YAG) fiber. The YAG fiber was initially grown from a pure YAG rod in <111> crystal orientation with a cross section of 50 mm x 50 mm by the laser-based drawing system.[64] □Optical microscope images of the YAG fiber are provided in Figure 5. The fiber's cross section reveals a hexagonally shaped facet with threefold symmetry, which is expected from a <111> cubic YAG crystal.[1,65] Cross-sectional TEM images (Figure 6) reveal a 200-300 nm thick layer of $FAPbBr_3$ along the YAG fiber surface. This is reinforced by energy-dispersive X-ray (EDX) mappings, which show good surface coverage for the $FAPbBr_3$@YAG fiber.

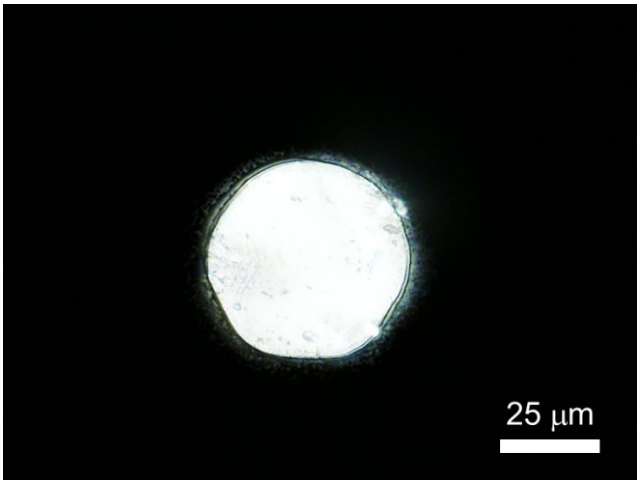

Figure 5. A cross-section optical microscope image of the YAG fiber.

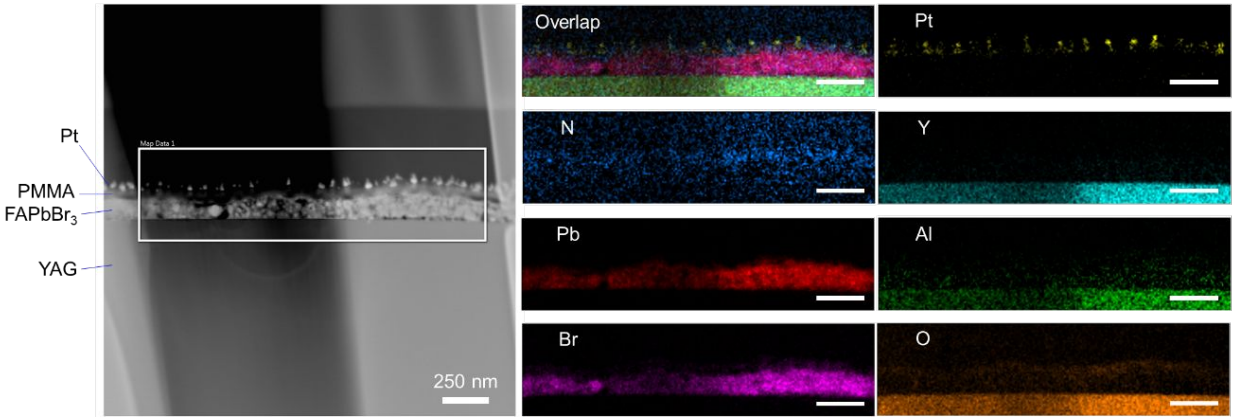

Figure 6. A cross-section optical microscope image of the $FAPbBr_3$@YAG fiber. Scale bars are 250 nm throughout the figure.

Figure 7 depicts the infrared spectra of $FAPbBr_3$@YAG under varying pressures. The $\delta NH_2/\nu_{as}CN$ band exhibits almost no pressure-induced changes in frequency for curves a-c (below 1 GPa), while a very subtle blue-shift and sharpening in bandwidth are evident for curves d-g (>1 GPa). Unfortunately, the N–H stretching bands have very low intensities when $FAPbBr_3$ is coated on the YAG optical fiber, and the low signal to noise ratios preclude an analysis of $FAPbBr_3$@YAG from the perspective of these vibrational modes. There are essentially no discernable differences in how the $\delta NH_2/\nu_{as}CN$ band responds to pressure when the YAG fiber is substituted with a sapphire fiber (Figure 7). These experimental findings provide some evidence that coating $FAPbBr_3$ on an optical fiber has a measurable impact on the structural stability of $FAPbBr_3$ up to a pressure of 2.5 GPa, and this observation aligns with previous results showing a marked improvement in the photostability of $FAPbBr_3$ when it is coated on the surface of an optical fiber.[1]

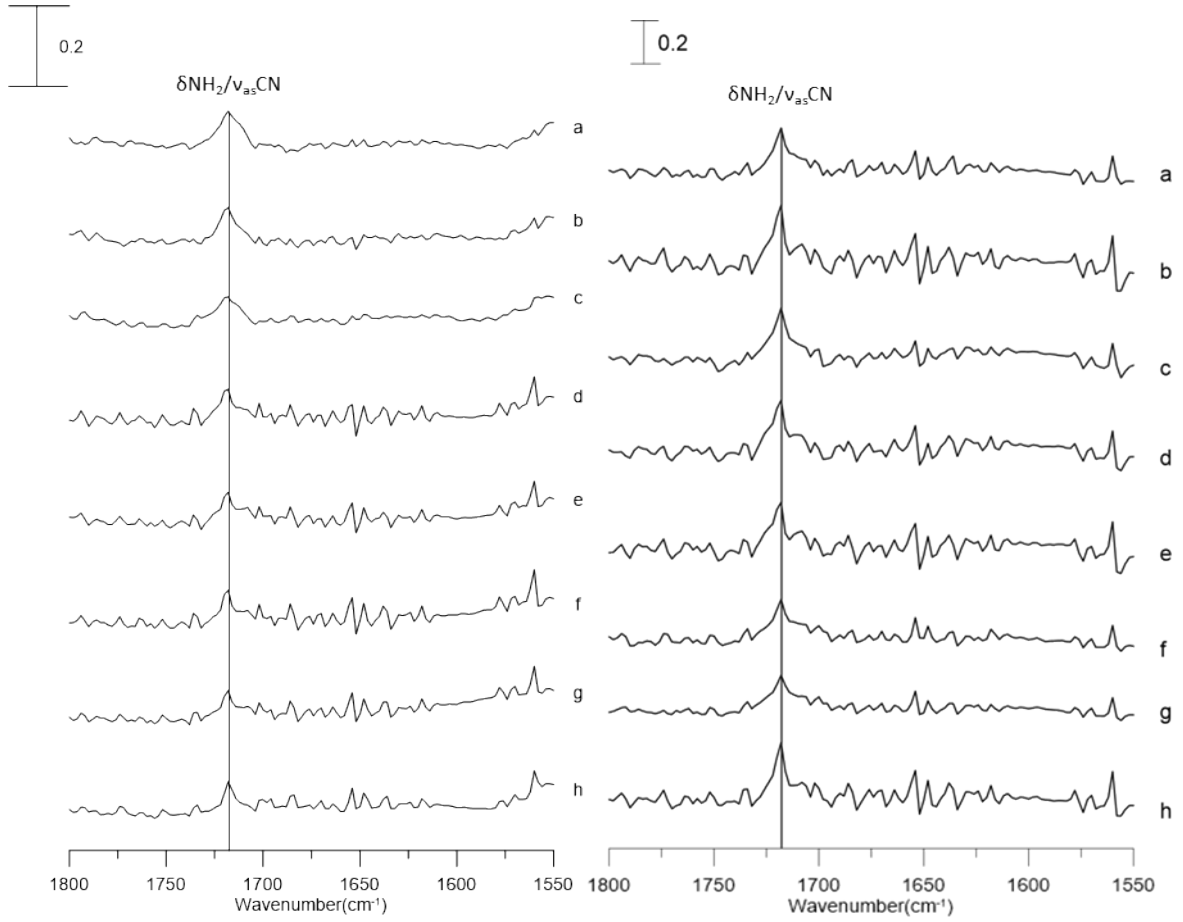

Figure 7. IR spectra of $FAPbBr_3$@YAG (left) and $FAPbBr_3$@sapphire at the pressure of (a) ambient, (b) 0.4, (c) 0.7, (d) 1.1, (e) 1.5, (f) 1.8, (g) 2.5 GPa, and (h) pressure cycling back to ambient. A relative intensity scale is provided in the upper left part of each panel.

The common feature of the PEEK and YAG experiments is that $FAPbBr_3$ is placed in configurations that emphasize interfacial impacts. Therefore, it is interesting to compare the how pressurization affects the FA^+ ions in two configurations and against the bulk form of $FAPbBr_3$. We focus on the $\delta NH_2/\nu_{as}CN$ band because it is discernable in all three samples. The band center wavenumber of $\delta NH_2/\nu_{as}CN$ is plotted as a function of applied pressure in Figure 8. Pure $FAPbBr_3$ exhibits a mild blue-shift upon compression in the range of ambient to 0.7 GPa. This is then followed by progressively larger red shifts when the sample is spectroscopically assessed at 1.1 GPa and higher pressures. The changes are consistent with the two known pressure-induced phase transitions for $FAPbBr_3$.[26,27] In particular, the spectroscopic data point to a subtle distortion in the $FAPbBr_3$ lattice at ~0.7 GPa, which leads to mild band shifts. Higher pressures induce noticeable changes in the IR absorption band. This is most likely due to a larger structural distortion. In the case of $FAPbBr_3$@PEEK, a red-shift of the $\delta NH_2/\nu_{as}CN$ band is also observed at the pressure of 1.1 GPa. However, there is no significant red-shift as the pressure is increased to 2.5 GPa for $FAPbBr_3$@PEEK.

Conversely, $FAPbBr_3$@YAG gives only a slight blue-shift of the $\delta NH_2/\nu_{as}CN$ across the entire pressure range. Thus, the spectroscopic transformation of $FAPbBr_3$ is somewhat different in each of these contexts, and coating $FAPbBr_3$ on the fiber surface appears to be a promising method for enhancing structural stability under high pressures. Based on the experimental results, the order of pressure-dependent structural modifications may be ranked as follows: pure $FAPbBr_3$ < $FAPbBr_3$@PEEK < $FAPbBr_3$@YAG.

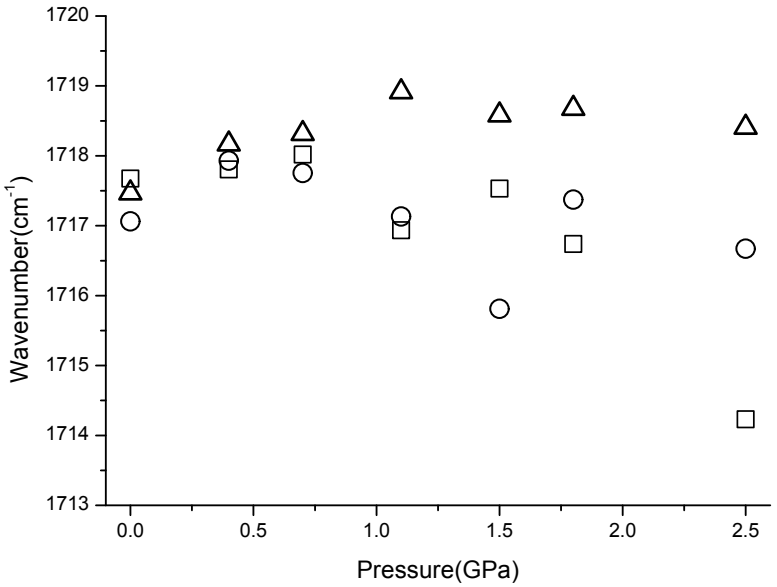

Figure 8. Pressure dependence of $\delta NH_2/\nu_{as}CN$ band for pure $FAPbBr_3$ (square), $FAPbBr_3$@PEEK (circle), and $FAPbBr_3$@YAG fiber (triangle).

Photoluminescence Studies on Confined and Coated $FAPbBr_3$

Figure 9 illustrates the photoluminescent properties of pure $FAPbBr_3$, $FAPbBr_3$@PEEK, and $FAPbBr_3$@YAG. All of the samples produce a single emission spectrum between 500 and 600 nm with band maxima at 545 nm ($FAPbBr_3$), 542 nm ($FAPbBr_3$@YAG), and 533 nm ($FAPbBr_3$@PEEK). The $FAPbBr_3$ sample experiences a rapid 90% decrease in photoluminescence intensity within 1 min of laser excitation. However, $FAPbBr_3$@PEEK maintains between 30% and 50% of its initial photoluminescence after 30 min of laser irradiation. The time-dependent photoluminescence of $FAPbBr_3$@YAG fiber exhibits an initial slight decrease in intensity, which recovers to ~80% of the intensity approximately 25 min after irradiation. Overall, the photoluminescence measurements suggest that the photo-stabilities of the samples follow the same order as the pressure dependent structural stabilizations discussed above.

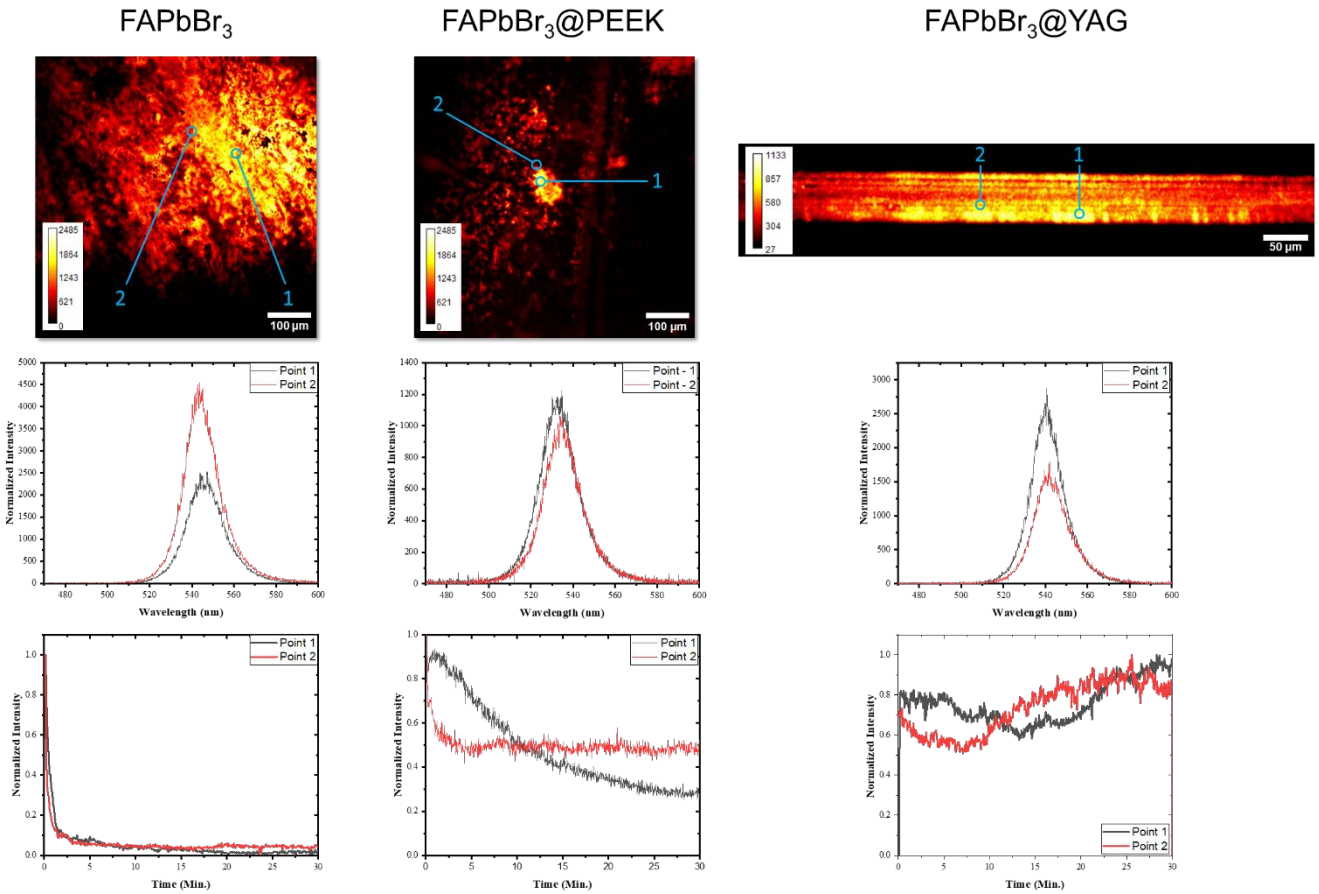

Figure 9. Photostability of pure $FAPbBr_3$, $FAPbBr_3$@PEEK, and $FAPbBr_3$@YAG. The top row contains photoluminescence images of the samples. The middle row depicts spectroscopic maps of the emitted electromagnetic radiation. The bottom row shows the temporal evolution of the total emitted intensity.

The mechanism of perovskite photoluminescence has aroused immense attention because of breakthroughs in perovskite applications.[66–69] Interfacial effects responsible for manipulating the photoluminescent properties are especially interesting. For example, Ivaniuk et al.[66] deposited $BaZrO_3$ pervoskite nanoparticles at the junction of two organic layers. Energy transfer between exciplexes across the organic layers and the $BaZrO_3$ via a Förster mechanism resulted in an organic/inorganic hybrid LED. The photoluminescence of $FAPbBr_3$ comes from exciton complexes and exciton-phonon coupling.[67] After optical excitation, various relaxation processes occur to produce the emitted electromagnetic radiation. A Jablonski-type diagram, which includes the conduction band, valence band, free electrons, and bounded excitons, summarizes the photophysical phenomenon for $FAPbBr_3$.[68] Interestingly, the frequency of $FAPbBr_3$ photoluminescence can be tuned across a wide range via size effects alone.[69] Nanocrystalline $FAPbBr_3$ delivers a size-dependent shift in the wavelength of the photoluminescent band maximum up to particle sizes of about 50

nm. At this point, the band frequency converges to the bulk $FAPbBr_3$ emission spectrum.[69] The band center wavelengths of our $FAPbBr_3$ and $FAPbBr_3$@YAG are approximately the same, but the band center for the $FAPbBr_3$@PEEK is noticeably smaller (533 nm). This is consistent with a smaller average particle size for the $FAPbBr_3$ crystallites in that sample.[69]

CONCLUSIONS

Comprehensive analysis of infrared spectra under different pressure conditions provides valuable insight into the dynamic behavior of $FAPbBr_3$ and its interactions with a confinement host or optical fiber. Ambient pressure IR spectroscopy is limited in its ability to detect the subtle local changes in $FAPbBr_3$ that occur when it is confined inside PEEK nanopores or coated on an optical fiber. However, these important factors become spectroscopically discernable at high pressure. The presence of PEEK membranes or YAG optical fibers appear to modify the phase behavior of $FAPbBr_3$, with pressure-dependent studies suggesting a hierarchy in structural stability: pure $FAPbBr_3$ < $FAPbBr_3$@PEEK < $FAPbBr_3$@YAG. This study also provides insight into the pressure-induced hydrogen bonding behavior of $FAPbBr_3$, especially under high pressures where stronger N–H···Br interactions are observed. The spectroscopic data is complemented by time-dependent photoluminescence measurements. These experiments reveal a clear increase in photoluminescence when $FAPbBr_3$ is placed in close contact with a substrate surface.

In summary, our findings underscore the importance of considering pressure effects when evaluating the structural stability of perovskite materials. The tailored confinement in PEEK and coating on optical fibers emerge as promising strategies to mitigate pressure-induced structural changes in $FAPbBr_3$ and offer new avenues for optimizing perovskite-based device performance under extreme conditions.

CReDiT Author Statement

Conceptualization: C.-C. Lai
Methodology: C.-C. Lai (photostability), H.-C. Chang (IR spectroscopy), C.M. Burba (computational analysis)
Validation: C.-C. Lai (photostability), H.-C. Chang (IR spectroscopy), C.M. Burba (computational analysis)
Formal Analysis: Y.-C. Chung (IR spectroscopy analysis), H. Y. T. Nguyen (photostability analysis), C.M. Burba (computational analysis)
Investigation: Y.-C. Chung (IR spectroscopy), H. Y. T. Nguyen (photostability)
Data Curation: H. Y. T. Nguyen (photostability), D. H. Nguyen (photostability), Y.-C. Chung (IR spectroscopy), C.M. Burba (computational analysis)
Writing – Original Draft: H.-C. Chang
Writing – Review & Editing: C.-C. Lai, H.-C. Chang, C.M. Burba

Visualization: Y.-C. Chung (IR spectroscopy), H. Y. T. Nguyen (photostability)
Supervision: C.-C. Lai (photostability), H.-C. Chang (IR spectroscopy), C.M. Burba (computational analysis)
Project Administration: H.-C. Chang
Funding Acquisition: C.-C. Lai, H.-C. Chang, C.M. Burba

Conflicts of Interest

The authors declare no conflicts of interest. The funders had no role in the design of the study; in the collection, analysis, or interpretation of data; in the writing of the manuscript; or in the decision to publish the results.

Acknowledgements

C.C.L. is grateful to the National Science and Technology Council of Taiwan (Contract No. NSTC 112-2112-M-259-018) for financial support. H.C.C. is grateful to the National Science and Technology Council of Taiwan (Contract No. NSTC 113-2113-M-259-006) for financial support. The authors thank Yu-Ting Chung for assistance with the project. Manuscript preparation was sponsored by the Office of Naval Research and was accomplished under Grant Number W911NF-23-1-0264 to C.M.B. The views and conclusions contained in this document are those of the authors and should not be interpreted as representing the official policies, either expressed or implied, of the Office of Naval Research or the U.S. Government. The U.S. Government is authorized to reproduce and distribute reprints for Government purposes notwithstanding any copyright notation herein.

References

1 D. H. Nguyen, J. Sun, C. Lo, J. Liu, W. Tsai, M. Li, S. Yang, C. Lin, S. Tzeng, Y. Ma, M. Lin and C. Lai, *Advanced Materials*, 2021, **33**, 2006819.

2 F. Zhao, A. Ren, P. Li, Y. Li, J. Wu and Z. M. Wang, *ACS Nano*, 2022, **16**, 7116–7143.

3 K. Wang, C. Huang, Q. Ruan, Y. Zhou, Y. Chen, H. Liu, S. Xiao and Q. Song, *ACS Photonics*, 2023, **10**, 2091–2101.

4 L. Gao, Y. Gong, X. Zhang, H. Yip, L. Shen and J. Zhang, *Laser Photon Rev*, DOI:10.1002/lpor.202301100.

5 Y.-L. Tong, Y.-W. Zhang, K. Ma, R. Cheng, F. Wang and S. Chen, *ACS Appl Mater Interfaces*, 2018, **10**, 31603–31609.

6 H. J. Jeong, C. Park, H. Jeon, K. N. Lee, J. Lee, S. C. Lim, G. Namkoong and M. S. Jeong, *ACS Appl Mater Interfaces*, 2021, **13**, 40891–40900.

7 B. Dridi Rezgui, I. Touhami, F. Khan, K. Ben Messaoud, C. Ben Alaya, Z. Antar and M. Bouaïcha, *Opt Mater (Amst)*, 2023, **135**, 113267.

8 X. Zhang, S. Zhang, Z. Ren, S. Wang, H. Liu, P. Wang, Z. Huang, R. Li and R. Chen,

iScience, 2024, **27**, 110794.

9 N. J. Schrenker, T. Braeckevelt, A. De Backer, N. Livakas, C. P. Yu, T. Friedrich, M. B. J. Roeffaers, J. Hofkens, J. Verbeeck, L. Manna, V. Van Speybroeck, S. Van Aert and S. Bals, *Nano Lett*, DOI:10.1021/acs.nanolett.4c02811.

10 K. Zhang, X. Zhang, K. G. Brooks, B. Ding, S. Kinge, Y. Ding, S. Dai and M. K. Nazeeruddin, *Solar RRL*, DOI:10.1002/solr.202300115.

11 J. Y. Sun, D. H. Nguyen, J. M. Liu, C. Y. Lo, Y. R. Ma, Y. J. Chen, J. Y. Yi, J. Z. Huang, H. Giap, H. Y. T. Nguyen, C. Da Liao, M. Y. Lin and C. C. Lai, *Advanced Science*, DOI:10.1002/advs.202301493.

12 G. E. Eperon, S. D. Stranks, C. Menelaou, M. B. Johnston, L. M. Herz and H. J. Snaith, *Energy Environ Sci*, 2014, **7**, 982–988.

13 J. Burschka, N. Pellet, S. J. Moon, R. Humphry-Baker, P. Gao, M. K. Nazeeruddin and M. Grätzel, *Nature*, 2013, **499**, 316–319.

14 N. J. Jeon, J. H. Noh, Y. C. Kim, W. S. Yang, S. Ryu and S. Il Seok, *Nat Mater*, 2014, **13**, 897–903.

15 C. Lin, *Frontiers Media S.A.*, 2020, preprint, DOI: 10.3389/fchem.2020.00592.

16 F. Ma, Y. Zhao, Z. Qu and J. You, *Acc Mater Res*, 2023, **4**, 716–725.

17 R. X. Yang, J. M. Skelton, E. L. Da Silva, J. M. Frost and A. Walsh, *Journal of Physical Chemistry Letters*, 2017, **8**, 4720–4726.

18 X. G. Zhao, G. M. Dalpian, Z. Wang and A. Zunger, *Phys Rev B*, DOI:10.1103/PhysRevB.101.155137.

19 C. Quarti, E. Mosconi, J. M. Ball, V. D'Innocenzo, C. Tao, S. Pathak, H. J. Snaith, A. Petrozza and F. De Angelis, *Energy Environ Sci*, 2016, **9**, 155–163.

20 G. Reuveni, Y. Diskin-Posner, C. Gehrmann, S. Godse, G. G. Gkikas, I. Buchine, S. Aharon, R. Korobko, C. C. Stoumpos, D. A. Egger and O. Yaffe, *Journal of Physical Chemistry Letters*, 2023, **14**, 1288–1293.

21 X. G. Zhao, Z. Wang, O. I. Malyi and A. Zunger, *Materials Today*, 2021, **49**, 107–122.

22 C. Gehrmann, S. Caicedo-Dávila, X. Zhu and D. A. Egger, *Advanced Science*, DOI:10.1002/advs.202200706.

23 E. C. Schueller, G. Laurita, D. H. Fabini, C. C. Stoumpos, M. G. Kanatzidis and R. Seshadri, *Inorg Chem*, 2018, **57**, 695–701.

24 A. M. Glazer, *Acta Crystallographica Section A*, 1975, **31**, 756–762.

25 A. M. Glazer, *Acta Crystallogr B*, 1972, **28**, 3384–3392.

26 L. Wang, K. Wang and B. Zou, *Journal of Physical Chemistry Letters*, 2016, **7**, 2556–2562.

27 X. Lou, L. Yao, N. Sui, Z. Kang, F. Li, Q. Zhou, Y. Li, M. Ni, H. Zhang and Y. Wang, *Journal of Physical Chemistry C*, 2021, **125**, 1041–1047.

28 F. H. Naqvi and J. H. Ko, *Journal of Raman Spectroscopy*, 2023, **54**, 1138–1149.

29 C.-H. Lin, T.-Y. Li, J. Zhang, Z.-Y. Chiao, P.-C. Wei, H.-C. Fu, L. Hu, M.-J. Yu, G. H. Ahmed, X. Guan, C.-H. Ho, T. Wu, B. S. Ooi, O. F. Mohammed, Y.-J. Lu, X. Fang and J.-H. He, *Nano Energy*, 2020, **73**, 104801.

30 M. Knezevic, T. H. Hoang, C. Wang, M. Johar, A. G. Manjón, D. L. Rauret, C. Scheu, M. Erard, D. Berardan, J. Arbiol, C. Colbeau-Justin and M. N. Ghazzal, *Adv Mater Interfaces*, DOI:10.1002/admi.202300636.

31 A. Maslavi, H. Unal and M. N. Olabi, *Wear*, DOI:10.1016/j.wear.2024.205464.

32 H. Huang, X. Liu, J. Wang, M. Suo, J. Zhang, T. Sun, H. Wang, C. Liu and Z. Li, *J Mater Chem B*, 2024, **12**, 4533–4552.

33 X. K. Dai, F. S. Yu, J. W. Wen, C. X. Wang, X. L. Ma, W. Yang, G. Y. Huang and H. M. Ye, *Chinese Journal of Polymer Science (English Edition)*, 2023, **41**, 1937–1946.

34 Y. Liu, Z. Zhang, X. Du, Y. Wang, X. Guo, M. Yu, B. Liu, W. Hu, L. Shen, Y. Lu and G. Zhu, *ACS Appl Mater Interfaces*, 2023, **15**, 37354–37360.

35 J. Liu, Y. Mo, S. Wang, S. Ren, D. Han, M. Xiao, L. Sun and Y. Meng, *ACS Appl Energy Mater*, 2019, **2**, 3886–3895.

36 T. Maharana, A. K. Sutar, N. Nath, A. Routaray, Y. S. Negi and B. Mohanty, in *Advanced Energy Materials*, eds. A. Tiwari and S. Valyukh, Wiley, 2014, pp. 433–464.

37 J. Pan, K. Li, J. Li, T. Hsu and Q. Wang, *Appl Phys Lett*, DOI:10.1063/1.3176219.

38 L. Hunger, R. Ludwig, Y. C. Chuang and H. C. Chang, *Journal of Physical Chemistry B*, 2024, **128**, 4802–4808.

39 L. Wang, K. Wang and B. Zou, *J Phys Chem Lett*, 2016, **7**, 2556–2562.

40 C. M. Burba, K.-Y. Hsiao, T.-H. Wang and H.-C. Chang, *J Mol Liq*, 2022, **365**, 120136.

41 N. Arora, M. I. Dar, M. Hezam, W. Tress, G. Jacopin, T. Moehl, P. Gao, A. S. Aldwayyan, B. Deveaud, M. Grätzel and M. K. Nazeeruddin, *Adv Funct Mater*, 2016, **26**, 2846–2854.

42 P. T. T. Wong and D. J. Moffatt, *Appl Spectrosc*, 1987, **41**, 1070–1072.

43 P. T. T. Wong, D. J. Moffatt and F. L. Baudais, *Appl Spectrosc*, 1985, **39**, 733–735.

44 F. Neese, *John Wiley and Sons Inc*, 2022, preprint, DOI: 10.1002/wcms.1606.

45 F. Neese, *WIREs Computational Molecular Science*, 2012, **2**, 73–78.

46 F. Neese, F. Wennmohs, U. Becker and C. Riplinger, *Journal of Chemical Physics*, DOI:10.1063/5.0004608.

47 F. Neese, *J Comput Chem*, 2023, **44**, 381–396.

48 E. F. Valeev, *http://libint.valeyev.net/*, 2024, preprint, http://libint.valeyev.net/:2.9.0.

49 A. D. Becke, *J Chem Phys*, 1993, **98**, 5648–5652.

50 B. Miehlich, A. Savin, H. Stoll and H. Preuss, *Chem Phys Lett*, 1989, **157**, 200–206.

51 C. Lee, W. Yang and R. G. Parr, *Phys Rev B*, 1988, **37**, 785–789.

52 A. Hellweg and D. Rappoport, *Physical Chemistry Chemical Physics*, 2015, **17**, 1010–1017.

53 P. Pulay, *J Comput Chem*, 1982, **3**, 556–560.

54 P. Pulay, *Chem Phys Lett*, 1980, **73**, 393–398.

55 V. Barone, M. Biczysko and J. Bloino, *Phys. Chem. Chem. Phys.*, 2014, **16**, 1759–1787.

56 F. Teixeira and M. N. D. S. Cordeiro, *J Chem Theory Comput*, 2019, **15**, 456–470.

57 E. Kucharska, J. Hanuza, A. Ciupa, M. Mączka and L. Macalik, *Vib Spectrosc*, 2014, **75**, 45–50.

58 A. G. Kontos, G. K. Manolis, A. Kaltzoglou, D. Palles, E. I. Kamitsos, M. G. Kanatzidis and P. Falaras, *Journal of Physical Chemistry C*, 2020, **124**, 8479–8487.

59 V. S. Rangasamy, S. Thayumanasundaram, J. W. Seo and J.-P. Locquet, *Spectrochim Acta A Mol Biomol Spectrosc*, 2015, **138**, 693–699.

60 C. Roth, S. Chatzipapadopoulos, D. Kerlé, F. Friedriszik, M. Lütgens, S. Lochbrunner, O. Kühn and R. Ludwig, *New J Phys*, 2012, **14**, 1–15.

61 J.-C. Lassègues, J. Grondin, D. Cavagnat and P. Johansson, *J Phys Chem A*, 2009, **113**, 6419–6421.

62 J.-C. Lassègues, J. Grondin, D. Cavagnat and P. Johansson, *J Phys Chem A*, 2010, **114**, 687–688.

63 J. Grondin, J.-C. Lassègues, D. Cavagnat, T. Buffeteau, P. Johansson and R. Holomb, *Journal of Raman Spectroscopy*, 2011, **42**, 733–743.

64 C.-C. Lai, C.-Y. Lo, J.-Z. Huang, C.-C. Fan Chiang, D. H. Nguyen, Y.-P. Chen and C.-D. Liao, *J Mater Chem C Mater*, 2018, **6**, 1659–1669.

65 C.-C. Lai, P. Yeh, S.-C. Wang, D.-Y. Jheng, C.-N. Tsai and S.-L. Huang, *The Journal of Physical Chemistry C*, 2012, **116**, 26052–26059.

66 K. Ivaniuk, V. Cherpak, P. Stakhira, G. Baryshnikov, B. Minaev, Z. Hotra, P. Turyk, Y. Zhydachevskii, D. Volyniuk, O. Aksimentyeva, B. Penyukh, A. Lazauskas, S. Tamulevičius, J. V. Grazulevicius and H. Ågren, *Dyes and Pigments*, 2017, **145**, 399–403.

67 K. Cho, T. Yamada, H. Tahara, T. Tadano, H. Suzuura, M. Saruyama, R. Sato, T. Teranishi and Y. Kanemitsu, *Nano Lett*, 2021, **21**, 7206–7212.

68 X. Geng, Y. Liu, X. Zou, E. M. J. Johansson and J. Sá, *Journal of Physical Chemistry C*, 2023, **127**, 3085–3092.

69 L. Protesescu, S. Yakunin, M. I. Bodnarchuk, F. Bertolotti, N. Masciocchi, A. Guagliardi and M. V. Kovalenko, *J Am Chem Soc*, 2016, **138**, 14202–14205.

All data supporting this article are included in the manuscript.